Applied Nanoscience (2020) 10:2867–2871
https://doi.org/10.1007/s13204-019-01142-x

ORIGINAL ARTICLE

TEM studies of structural defects in HgTe/HgCdTe quantum wells

O. Yu. Bonchyk[1] · H. V. Savytskyy[1] · Z. Swiatek[2] · Y. Morgiel[2] · I. I. Izhnin[3,4] · A. V. Voitsekhovskii[4] · A. G. Korotaev[4] · K. D. Mynbaev[5] · O. I. Fitsych[6] · V. S. Varavin[7] · S. A. Dvoretsky[4,7] · N. N. Mikhailov[7] · M. V. Yakushev[7]

Received: 21 December 2018 / Accepted: 19 August 2019 / Published online: 10 September 2019

Abstract
Bright-field and high-resolution transmission electron microscopy and microdiffraction have been used for the study of defects in two HgTe/HgCdTe single quantum well (QW) structures grown by molecular beam epitaxy on GaAs substrates with ZnTe and CdTe buffer layers. Defects in QW layers were identified as stacking faults, dislocations, dislocation loops and lattice deformations. The importance of an extra HgCdTe layer placed between the CdTe buffer and HgTe/HgCdTe QW structure for the reduction of defect density both in the barrier layers and in the well itself was demonstrated.

Keywords HgCdTe · Quantum wells · Transmission electron microscopy · Defects

Background

Recently, HgTe/HgCdTe quantum wells (QWs) have been studied intensively due to their unique properties and the resulting applications. One of their features, for example, is the change of band ordering with the variation of the width of the well (Krishtopenko and Teppe 2018; Bernevig et al. 2006). QWs with the inverted band ordering were identified and studied as 2D topological insulators (Buttner et al. 2011; Konig et al. 2007), while narrow-bandgap HgTe/HgCdTe QWs with normal band ordering represent strong interest for far-infrared opto- and photo-electronics and terahertz photonics (Aleshkin et al. 2018; Ruffenach et al. 2017).

Molecular beam epitaxy (MBE) of HgTe-related compounds allows for growing Hg(Cd)Te structures not only on 'native' Cd(Zn)Te substrate, but also on "alternative" substrates made of GaAs, Si, Ge, and GaSb (Gu et al. 2016). These substrates are less expensive and have a much larger area than those made of Cd(Zn)Te. GaAs substrates provide very good balance between size and cost, on the one hand, and lattice mismatch and difference between the thermal expansion coefficients of Hg(Cd)Te and the substrate, on the other. However, dislocation density in HgCdTe epitaxial films grown on GaAs is about two orders of magnitude higher than that in the films grown on CdZnTe (Sidorov et al. 2015). This inevitably affects the concentration of defects in all the layers of HgCdTe-based heterostructures grown on GaAs, and eventually, the properties of the resulting device. The structural defects in Hg(Cd)Te-based QWs grown on 'alternative' substrates, to the best of our knowledge, so far have not been studied with electron microscopy. In this work, we report on the results of a study of the defects carried out with transmission electron microscopy (TEM) on two HgTe/HgCdTe single-QW structures with different designs grown by MBE on GaAs(013) substrates.

✉ O. Yu. Bonchyk
bonchyk@ukr.net

1 Ya. S. Pidstryhach Institute for Applied Problems of Mechanics and Mathematics NASU, Naukova 3b, Lviv 79060, Ukraine

2 Institute of Metallurgy and Material Science PAN, Reymonta 25, 30-059 Kraków, Poland

3 Scientific Research Company "Electron-Carat", Striiskaya 202, Lviv 79031, Ukraine

4 National Research Tomsk State University, Lenina 36, Tomsk 634050, Russia

5 ITMO University, Kronverkskiy 49, Saint-Petersburg 197101, Russia

6 Hetman Petro Sahaidachny National Army Academy, Gvardijska 32, 79012 Lviv, Ukraine

7 A. V. Rzhanov Institute of Semiconductor Physics, SB RAS, Ac, Lavrentieva 13, Novosibirsk 630090, Russia

Methods

Growth was performed with the use of ZnTe and CdTe buffers with in situ ellipsometric control of chemical composition and thickness of all the layers (Dvoretsky et al. 2010). Figure 1a, c shows schematics of the samples studied, starting from the CdTe buffer layer at the bottom of the drawing and finishing with the CdTe protective surface layer at the top. The thickness of the ZnTe buffer layer in both structures was 30 nm (this layer is not shown in Fig. 1), that of the CdTe buffer layer, 5.6 µm. The CdTe buffer layers were grown with the growth rate 2 µm/h, the growth rate for HgTe QWs was 0.05 nm/s. Sample #1 shown in Fig. 1a, b differed from sample #2 (Fig. 1c, d) in that the former contained an extra 'buffer' HgCdTe layer (designated as ***D***) between the CdTe buffer layer and the first HgCdTe barrier layer. The structures also slightly differed in chemical composition of the barrier layers as shown in Fig. 1a, c. The barriers were delta-doped with indium with concentration ~ 3×10^{16} cm^{-3} in sample #1, and ~ 1×10^{17} cm^{-3}, in sample #2. Both QWs were set to have 8 nm widths.

Structural defects were studied with TEM in bright-field (BF TEM) and high-resolution (HRTEM) modes using Tecnai G2 F20, FEI Company microscope. Thin foils for TEM and HRTEM observations were cut out using FEI Quanta 200 dual-beam focused ion (Ga^+) beam (FIB) machine equipped with Omniprobe™ lift-out system. The investigated material was first covered with 300 nm-thick amorphous carbon layer that prevented the surface from the damage that could be inflicted by Ga^+ ions used for the deposition of a Pt bar. Next, trench milling was done on both sides of the bar. Here, the effect of Ga^+ ions was minimized by limiting the gallium beam current during the milling, starting from 20 nA, continuing with 7 nA, and finishing with 5 nA. The final polishing of the lifted lamella was done starting from 1 nA ion beam current, continuing with 0.3 nA, and finishing with 0.1 nA. The energy of Ga^+ ions did not exceed 2 keV. The use of FIB sample preparation technique with trench milling (in contrast to traditional method where ion milling is applied directly to the studied plane) strongly suppresses the generation of defects resulting from ion damage, such as dislocations (Vaghayenegar et al. 2017), and helps to avoid milling-induced artifacts in the course of TEM studies. This was demonstrated, for example, in the studies of nano-size defects in arsenic-implanted HgCdTe films before and after thermal annealing (Bonchyk et al. 2019).

Results and discussion

The difference in chemical compositions of layers results in different contrasts in a TEM image, which allows for identifying individual layers in the image of a multi-layer

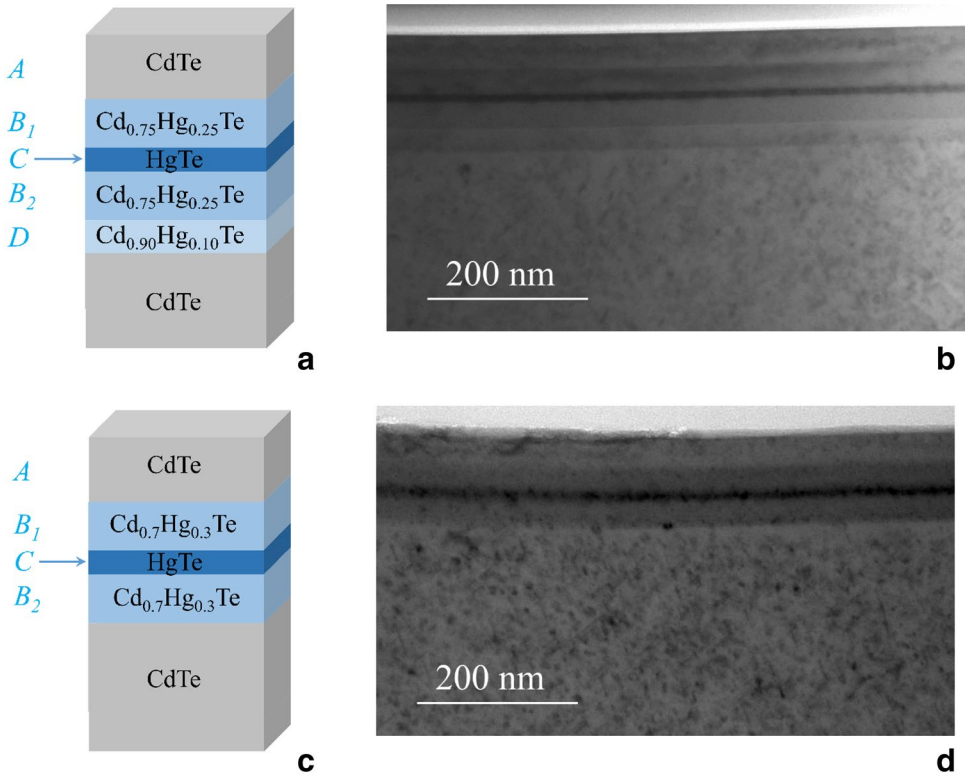

Fig. 1 Schematics of the design **a, c** and BF TEM review images **b, d** of the cross-sections of sample #1 **a**, **b** and sample #2 **c, d**

structure. Processing of the obtained images showed that the actual thicknesses of the layers in both samples were in a good agreement with their design (see Table 1). The thicknesses of the QWs, according to the TEM data, appeared to be 10 nm.

Figure 2 shows BF TEM images of the cross-sections of both samples obtained with higher, as compared to Fig. 1, magnification. Images in Figs. 1b, d and 2 clearly show the layered structure of the samples, and density of defects is obviously different in different layers.

Analysis of various TEM images acquired from sample #1, including one shown in Fig. 2a showed that in layer ***A*** defects were located in the middle part of the layer. In contrast to this, structural defects in layer $\boldsymbol{B_1}$ were mostly located near the $\boldsymbol{A/B_1}$ interface. In layer ***C*** (HgTe QW) defects were distributed uniformly along its thickness. Layer $\boldsymbol{B_2}$, similar to layer $\boldsymbol{B_1}$, contained defects near the interface with the adjusting layer, in this case it was the $\boldsymbol{B_2/D}$ interface. The $\boldsymbol{B_2/D}$ interface also seemed to be not as sharp as the others, as it showed low contrast in the images. Layer ***D*** had defects throughout its whole depth, and its interface with the CdTe buffer layer showed a large density of structural defects. In the whole sample, the highest density of defects was found in the CdTe buffer layer. For $\boldsymbol{B_1}$ and $\boldsymbol{B_2}$ layers, no structural defects associated with indium doping were found (a similar observation for indium-doped HgCdTe was made by Kim et al. (2012) and Wang et al. (2006)).

Figure 2b shows structural defects in sample #2. It is seen in Fig. 2 that the CdTe buffer layers in both samples contained very high density of defects, and this density seemed to be similar for samples #1 and #2. This effect must be caused by the 'foreign' GaAs substrate: the strong lattice mismatch between the substrate and the epitaxial layers resulted in such a high density of structural defects that even relatively thick CdTe buffer layer was incapable to compensate for it. However, the extra 'buffer' layer ***D***, which was present in sample #1, still seemed to serve as a barrier for the propagation of defects accumulated in the CdTe buffer layer. In Fig. 2a, one can see that the concentration of defects reduces throughout the depth of layer ***D*** and further up, crossing the interface and going deeper into layer $\boldsymbol{B_2}$. Some increase in the concentration of defects in layer ***C*** (HgTe QW) is probably conditioned by the presence of $\boldsymbol{B_2/C}$ and $\boldsymbol{C/B_1}$ interfaces and changes in growth mode when transitioning from one material to another since the lattice mismatch between HgTe and CdTe is very small (0.3%). This effect is probably also responsible for the specifics of defect structure of layer $\boldsymbol{B_1}$, which appears to be almost free of defects in the middle of the layer with the density of defects increasing at both interfaces, $\boldsymbol{C/B_1}$ and $\boldsymbol{B_1/A}$.

By comparing two images shown in Fig. 2, one can conclude that layer $\boldsymbol{B_2}$ in sample #1 had lower defect density than the similar layer in sample #2 and that layers ***C*** in samples #1 and #2 differed in their defect structure. In sample #1, the defects appeared to be located strictly within layer ***C*** itself, while in sample #2 they seemed to be scattered across a larger area, being present also in layers $\boldsymbol{B_1}$ and $\boldsymbol{B_2}$. As a result of this, layer ***C*** in sample #2 visibly (in the TEM

Table 1 Thicknesses of layers in the studied samples

Layer	Sample #1			Sample #2		
	Composition	Thickness set, nm	Thickness by TEM, nm	Composition	Thickness set, nm	Thickness by TEM, nm
A	CdTe	40	40	CdTe	40	40
$\boldsymbol{B_1}$	$Cd_{0.75}Hg_{0.25}Te$	30	30	$Cd_{0.70}Hg_{0.30}Te$	30	32
C	HgTe	8	10	HgTe	8	10
$\boldsymbol{B_2}$	$Cd_{0.75}Hg_{0.25}Te$	30	30	$Cd_{0.70}Hg_{0.30}Te$	30	32
D	$Cd_{0.90}Hg_{0.10}Te$	20	36	–	–	–

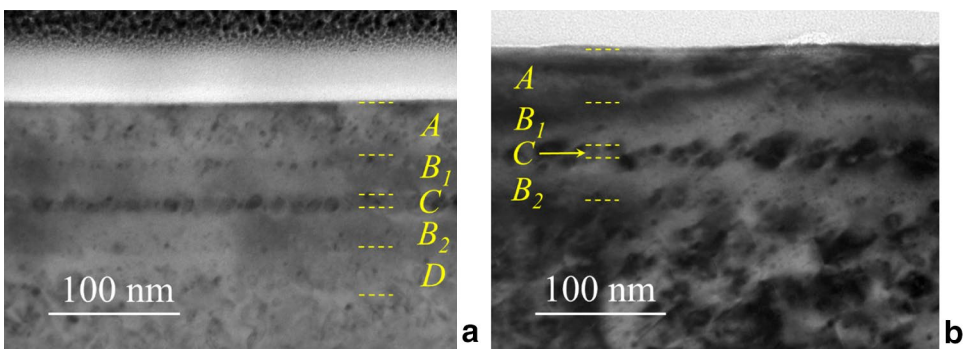

Fig. 2 Cross-sectional BF TEM images of the QW structure in sample #1 **a** and sample #2 **b**. Letters in the images designate layers as shown in Fig. 1

images) appeared to be 'thicker' than that in sample #1, and defects in this layer appeared to be larger in size than those in sample #1.

The detailed studies of defects in layers ***C*** in both samples were performed with the use of HRTEM with Fast Fourier Transform (FFT) and Inverse Fast Fourier Transform (IFFT) processing of the images. This numerical image processing technique allows for measuring the local shifts of image details around a crystal defect with respect to the ideal, defect-free, position, and in HgCdTe technology has been successfully used for the studies of structural defects in, e.g., CdTe/GaAs(Si) substrates for HgCdTe growth (Kim et al. 2013) and HgCdTe epitaxial films subjected to ion implantation (Bonchyk et al. 2019).

Figure 3a shows a HRTEM image that demonstrates the structure of a typical defect area in layer ***C*** of sample #1. Two major visible defect elements are marked as $\boldsymbol{P_1}$ and $\boldsymbol{P_2}$, respectively. Inset shows a microdiffraction pattern of the studied area. IFFT images of the areas associated with the selected elements are shown in Fig. 3b, c ({111} crystallographic plane). In these images, one can clearly see dislocations (marked with arrows), stacking faults and lattice deformations (solid ovals) and dislocation loops (dashed ovals).

Figure 4a shows a HRTEM image of a typical defect area in layer ***C*** of sample #2. Two major visible defect elements are similarly marked as $\boldsymbol{P_1}$ and $\boldsymbol{P_2}$. The insets in image (**a**) show microdiffraction patterns of the studied areas. IFFT images of the areas associated with the selected elements are shown in Fig. 4b, c. In these images, one can again see dislocations (marked with arrows), stacking faults and lattice deformations (solid ovals) and dislocation loops (double arrows and dashed ovals). The size of the latter marked with the dashed ovals was estimated to be 6 nm for the smaller loop in Fig. 4b, and 11 nm, for the bigger loop in Fig. 4c. The layers also had smaller dislocation loops, but the dominating defects were single dislocations and stacking faults. The defects

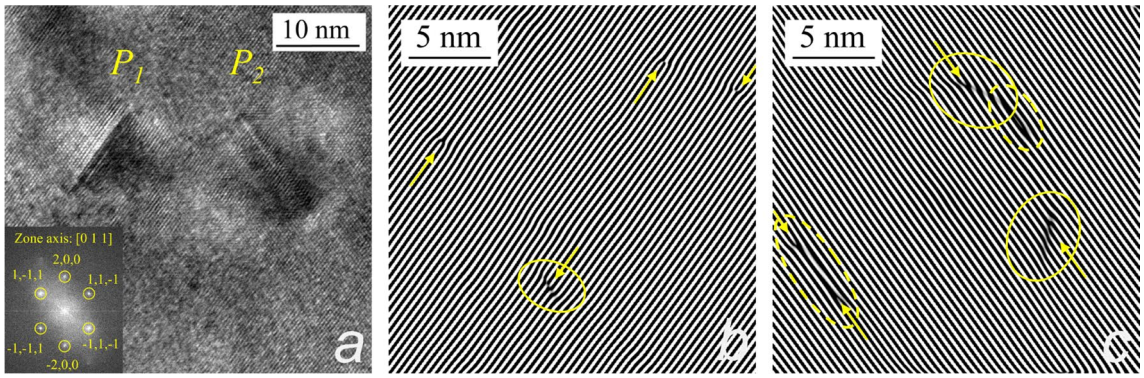

Fig. 3 High-resolution TEM image of a fragment of layer ***C*** in sample #1 (**a**), and IFFT images of the elements of its defect structure $\boldsymbol{P_1}$ (**b**) and $\boldsymbol{P_2}$ (**c**). Inset in image (**a**) shows a microdiffraction pattern. Defects in IFFT images are marked with: dislocations, arrows; stacking faults and lattice deformations, solid ovals; dislocation loops, dashed ovals

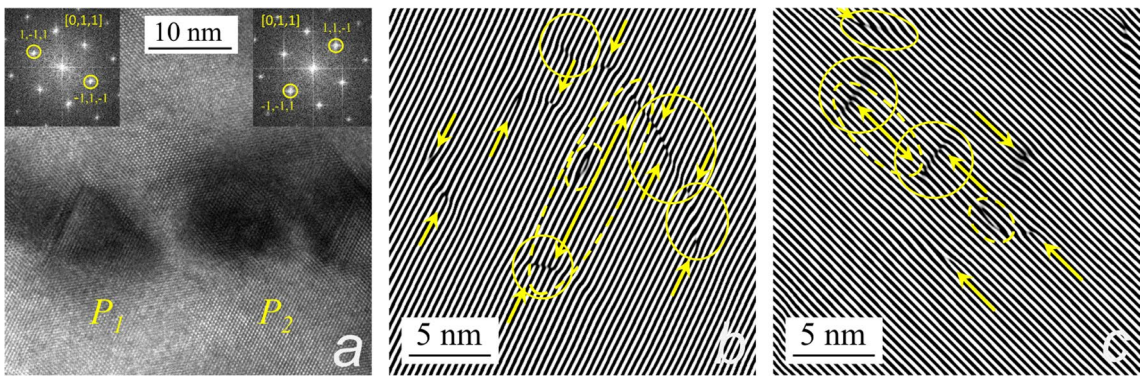

Fig. 4 High-resolution TEM image of a fragment of layer ***C*** in sample #2 (**a**), and IFFT images of the elements of its defect structure $\boldsymbol{P_1}$ (**b**) and $\boldsymbol{P_2}$ (**c**). Insets in image (**a**) show diffraction patterns for the elements $\boldsymbol{P_1}$ (left inset) and $\boldsymbol{P_2}$ (right inset). Defects in IFFT are marked with: dislocations, single arrows; stacking faults and lattice deformations, solid circles/ovals; dislocation loops, double arrows and dashed ovals

produced lattice deformations, which are visible as darkened areas in IFFT images and are marked with solid circles and ovals.

Comparing Figs. 4 and 3, one can again notice that layer ***C*** in sample #2 contains larger number of defects than layer ***C*** in sample #1. The analysis of IFFT images for larger areas for both samples (not shown) also revealed that layer ***C*** in sample #2 had higher concentration of defects at the C/B_1 and C/B_2 interfaces. In addition to this, defects in layer ***C*** in sample #2 appeared to be more complex than those in layer ***C*** in sample #1, and some HRTEM images of sample #2 showed increased defect density at the C/B_2 interface. The reason for the high defect concentration at the C/B_2 interface in sample #2 should be related to higher defect concentration in layer B_2, which served as a 'substrate' for layer ***C***. This, in its turn, should be related to the absence of the extra 'buffer' layer ***D*** in this sample.

It appears that the following conclusions can be drawn: (i) both HgTe/HgCdTe QW samples had quite high density of defects in the 'main' CdTe buffer layer, which might indicate a necessity to optimize growth conditions for this layer; (ii) layer B_2, which was adjacent to the QW layer ***C*** from the side of the substrate, in sample #1 had lower density of defects than the similar layer in sample #2; (iii) layer ***C*** in sample #2 contained defects larger in size, with higher density and more complex in structure than the similar layer in sample #1; and (iv) layers B_1 and ***A***, the top layers of the QW structures, in sample #1 also had lower density of defects than their counterparts in sample #2. Therefore, the presence of layer ***D*** as an extra 'buffer' layer appeared to be very important, as it reduced the density and size of defects in all the layers of the heterostructure, including the QW. Note that defects revealed and identified in this TEM study, namely, dislocations, dislocation loops and lattice deformations, appear to be typical of MCT grown by MBE. The only factors that vary from layer to layer are the density of these defects and their dimensions.

Conclusion

In conclusion, bright-field and high-resolution transmission electron microscopy were used for the study of two HgTe/HgCdTe single quantum well (QW) structures (QW thickness ~ 10 nm) grown by molecular beam epitaxy on GaAs substrate with ZnTe and CdTe buffer layers. Both structures appeared to have a high density of defects in the CdTe buffer layer located between the ZnTe layer grown on the GaAs substrate and the QW structure. The density of defects and their distribution in other layers strongly depended on the presence or the absence of an extra HgCdTe 'buffer' layer between the CdTe buffer layer and the QW structure. Defects in the QWs were identified as stacking faults, dislocations, dislocation loops and defect-induced lattice deformations. In total, the presence of an extra HgCdTe 'buffer' layer with chemical composition value in between that of the CdTe buffer layer and that of barrier layers in QW structure appeared to be very important, as it defined the quality of the whole heterostructure. Inserting such a layer certainly is a simple and inexpensive technique that can provide a great gain in the crystal quality of HgTe/HgCdTe QW structures.

Compliance with ethical standards

Conflict of interest On behalf of all authors, the corresponding author states that there is no conflict of interest.

References

Aleshkin VY, Dubinov AA, Morozov SV et al (2018) Interband infrared photodetectors based on HgTe-CdHgTe quantum-well heterostructures. Opt Mater Express 8:1349–1358

Bernevig BA, Hughes TL, Zhang SC (2006) Quantum spin Hall effect and topological phase transition in HgTe quantum wells. Science 314:1757–1761

Bonchyk OYu, Savytskyy HV, Swiatek Z et al (2019) Nano-size defects in arsenic-implanted HgCdTe films: a HRTEM study. Appl Nanosci 9:725–730

Buttner B, Liu CX, Tkachov G et al (2011) Single valley Dirac fermions in zero-gap HgTe quantum wells. Nat Phys 7:418–422

Dvoretsky S, Mikhailov N, Sidorov Yu et al (2010) Growth of HgTe quantum wells for IR to THz detectors. J Electron Mater 39:918–923

Gu RJ, Lei W, Antoszewski J et al (2016) Investigation of substrate effects on interface strain and defect generation in MBE-grown HgCdTe. J Electron Mater 45:4596–4602

Kim KC, Baek SH, Kim HJ et al (2012) A structural investigation of CdTe(001) thin films on GaAs/Si(001) substrates by high-resolution electron microscopy. J Electron Mater 41:2795–2798

Kim JJ, Jacobs RN, Almeida LA et al (2013) TEM characterization of HgCdTe/CdTe grown on GaAs(211)B substrates. J Electron Mater 42:3142–3147

Konig M, Wiedmann S, Brüne C et al (2007) Quantum spin hall insulator state in HgTe quantum wells. Science 318:766–770

Krishtopenko SS, Teppe F (2018) Realistic picture of helical edge states in HgTe quantum wells. Phys Rev B 97:165408

Ruffenach S, Kadykov A, Rumyantsev VV et al (2017) HgCdTe-based heterostructures for terahertz photonics. APL Mater 5:035503

Sidorov Y, Yakushev MV, Varavin VS et al (2015) Density of dislocations in CdHgTe heteroepitaxial structures on GaAs(013) and Si(013) substrates. Phys Solid State 57:2151–2158

Vaghayenegar M, Jacobs RN, Benson JD et al (2017) Correlation of etch pits and dislocations in as-grown and thermal cycle-annealed HgCdTe(211) films. J Electron Mater 46:5007–5019

Wang C, Tobin S, Parodos T et al (2006) Investigation of HgCdTe *p–n* device structures grown by liquid-phase epitaxy. J Electron Mater 35:1192–1196